



EMPIRICALLY ESTIMATED FAR-UV EXTINCTION CURVES FOR CLASSICAL T TAURI STARS

MATTHEW MCJUNKIN¹, KEVIN FRANCE¹, REBECCA N. SCHINDHELM², GREGORY HERCZEG³, P. CHRISTIAN SCHNEIDER⁴, AND ALEX BROWN⁵¹ Laboratory for Atmospheric and Space Physics, University of Colorado, 600 UCB, Boulder, CO 80303-7814, USA; matthew.mcjunkin@colorado.edu² Southwest Research Institute, 1050 Walnut Street, Suite 300, Boulder, CO 80302, USA³ Kavli Institute for Astronomy and Astrophysics, Peking University, Yi He Yuan Lu 5, Haidian Qu, 100871 Beijing, China⁴ ESA/ESTEC, Keplerlaan 1, 2201 AZ Noordwijk, The Netherlands⁵ Center for Astrophysics and Space Astronomy, University of Colorado, 593 UCB, Boulder, CO 80309-0593, USA

Received 2016 January 12; revised 2016 June 13; accepted 2016 June 29; published 2016 September 1

ABSTRACT

Measurements of extinction curves toward young stars are essential for calculating the intrinsic stellar spectrophotometric radiation. This flux determines the chemical properties and evolution of the circumstellar region, including the environment in which planets form. We develop a new technique using H₂ emission lines pumped by stellar Ly α photons to characterize the extinction curve by comparing the measured far-ultraviolet H₂ line fluxes with model H₂ line fluxes. The difference between model and observed fluxes can be attributed to the dust attenuation along the line of sight through both the interstellar and circumstellar material. The extinction curves are fit by a Cardelli et al. (1989) model and the $A_V(H_2)$ for the 10 targets studied with good extinction fits range from 0.5 to 1.5 mag, with R_V values ranging from 2.0 to 4.7. A_V and R_V are found to be highly degenerate, suggesting that one or the other needs to be calculated independently. Column densities and temperatures for the fluorescent H₂ populations are also determined, with averages of $\log_{10}(N(H_2)) = 19.0$ and $T = 1500$ K. This paper explores the strengths and limitations of the newly developed extinction curve technique in order to assess the reliability of the results and improve the method in the future.

Key words: circumstellar matter – dust, extinction – ISM: molecules – protoplanetary disks – stars: variables: T Tauri, Herbig Ae/Be – ultraviolet: ISM

1. INTRODUCTION

The protoplanetary disk environment regulates the type of planets that can form around a young star. The stellar radiation, specifically the ultraviolet (UV) radiation, plays a strong role in chemical heating (Jonkheid et al. 2004; Nomura et al. 2007; Woitke et al. 2009) and processing (Aikawa & Herbst 1999; Bethell & Bergin 2009; Fogel et al. 2011; Bruderer 2013) in the disk. The interstellar and circumstellar media, however, can absorb the stellar radiation along the line of sight and change the observed spectral energy distribution (SED). Characterizing the extinction allows us to recover the intrinsic stellar SED in order to better understand the environment of planet formation around these objects.

The canonical interstellar curve of Cardelli et al. (1989) describes the wavelength dependence of interstellar extinction using the color excess ($E(B - V)$) value and the R_V parameter, which depends on the grain size distribution ($R_V = A_V/E(B - V)$, with A_V being the visual extinction). The extinction curve is described by the formula $A_\lambda/A_V = a(x) + b(x)/R_V$ (where $x = 1/\lambda$), which is broken up into four regions (infrared, optical/NIR, mid-UV, and far-UV), with unique polynomial parameterizations of $a(x)$ and $b(x)$. The diffuse interstellar medium (ISM) has a canonical R_V value of 3.1 (Rieke & Lebofsky 1985). In protoplanetary disk environments, grain growth can lead to non-interstellar dust populations and different gas-phase abundances. Simulations of dust populations in disks have been performed by Birnstiel et al. (2012), showing that turbulence in disks is necessary to explain the small grain population observed. The turbulence increases the collision rate, which helps create new small grains from larger grains. Vasyunin et al. (2011) argue that, although disk grain growth allows UV photons to penetrate more easily into

the disk interior, it also leads to increased gas-phase molecular column densities due to the reduction of the total grain surface.

Extinction curves with larger R_V values indicate grain populations with more large grains and fewer small grains, such as the $R_V \sim 5.6$ typical of dense molecular clouds (Cardelli et al. 1989). Allen et al. (2014) find an extinction curve toward the young cluster Cep OB3b that is intermediate between the $R_V = 3.1$ law used for the diffuse atomic ISM and the $R_V \sim 5.6$ law used for dense molecular clouds. Due to the observed variation in R_V along the line of sight toward different targets, measuring the correct extinction curve toward individual targets is crucial for reconstructing their intrinsic SED. Circumstellar grain growth can also affect the extinction curve such that the shape is no longer well described by the parameterization of Cardelli et al. (1989). In this case, the extinction curve has both interstellar and circumstellar components, with the line of sight passing through multiple different dust grain populations. In such a case, an empirically derived extinction curve is required.

Typically, line-of-sight extinction curves are measured via the pair method by comparing the SED of a reddened star to the SED of another star with similar properties but little to no reddening (Rudnick 1936). This method assumes that we can find an unreddened star that is similar enough to the star we are studying. More recently, Fitzpatrick & Massa (2005) have created a method to determine extinction curves using a stellar atmosphere model to create the unreddened SED rather than using an unreddened standard star. This method relies on having an accurate spectral type of the target star in order to create an accurate unreddened model spectrum of the same type. However, this method cannot be applied to young, classical T Tauri stars (CTTSs) because the wavelength-dependent veiling from excess accretion emission (e.g.,

Gullbring et al. 1998) cannot currently be predicted with sufficient accuracy to derive reliable stellar masses and radii (Hartigan et al. 1995).

In this paper, we present a novel technique using H_2 line emission from the surface of the protoplanetary disk to constrain the wavelength-dependent attenuation toward CTTSs. We analyze the results and explore the limitations in order to improve the method in future work. Comparing H_2 fluorescent line fluxes with theoretical models allow us to calculate an extinction curve between 1100 and 1700 Å. The broad $\text{Ly}\alpha$ profile of a protostar pumps H_2 electronic transitions, which then fluoresce in the UV. Previous work modeling H_2 fluorescence in different targets and/or different techniques has been calculated by Wood et al. (2002), Herczeg et al. (2004, 2005), France et al. (2012b), and Hoadley et al. (2015). We use a reconstructed $\text{Ly}\alpha$ profile (e.g., Schindhelm et al. 2012b) to pump the H_2 molecules and model the predicted fluorescence spectrum. Differences between the observed and theoretical H_2 fluorescence lines indicate attenuation occurring along the line of sight. This attenuation is caused by dust extinction and self-absorption in the interstellar and circumstellar media. The effects can be separated using the derived properties of the emitting H_2 populations.

Our measurement of the attenuation of UV photons by dust as a function of wavelength requires several steps:

- Column density and temperature fit—We fit the long-wavelength UV lines ($1450 \text{ Å} < \lambda < 1620 \text{ Å}$) where self-absorption is negligible by using the reconstructed $\text{Ly}\alpha$ profiles of Schindhelm et al. (2012b) and France et al. (2014) to excite the H_2 molecules. For a grid of column densities and temperatures, we compute the ground-state H_2 populations and calculate the resulting fluorescent cascade. The minimum difference between the line fluxes of the model and the data gives the best-fit parameters.
- Construct an initial attenuation curve—Dividing the observed line fluxes by the predicted line fluxes over the full wavelength range gives an initial curve showing the absorption occurring between the location of the H_2 fluorescence and our observations from the *Hubble Space Telescope* (HST). This attenuation can be attributed to interstellar and circumstellar extinction as well as to self-absorption of the H_2 molecules, so we must next correct for the self-absorption in order to characterize the extinction.
- Self-absorption correction—To account for H_2 self-absorption in the disk, we find the transmission of each rovibrational transition at the best-fit column density and temperature. The transmission determines the amount of self-absorption that occurs, so we divide each line by its transmission value to determine the extinction curve.
- A_V and R_V fit—Searching a grid of A_V and R_V values and assuming a standard ISM extinction curve of Cardelli et al. (1989), we find the best-fit parameters for our self-absorption-corrected extinction curve.

Section 2 presents the targets and observations used in this work. The H_2 fluorescence process is discussed in Section 3. The H_2 fluorescence models, self-absorption correction, and fits to A_V – R_V extinction curves are described in detail in Section 4. Section 5 contains the results of all of the model fits, and is followed by a discussion in Section 6 comparing our work with previous extinction work as well as an exploration of the

limitations of this new technique. We finish with a summary in Section 7.

2. TARGETS AND OBSERVATIONS

We analyze the UV spectra of 16 young stars, which are a subset of the targets studied in McJunkin et al. (2014). These targets are chosen because they have $\text{Ly}\alpha$ profiles reconstructed from Schindhelm et al. (2012b) and France et al. (2014), which we use to pump the H_2 molecules in our fluorescence model. The majority of the targets are in the Taurus–Auriga star-forming region, with a few from the η Chamaeleontis star-forming region or field stars. The ages of the young stars calculated by placing individual stars on H–R diagrams range from 1 to 30 Myr, but most of the targets are 1–10 Myr old.

The majority of the data were obtained using the *HST* Cosmic Origins Spectrograph (HST-COS). The TW Hya data are archival Space Telescope Imaging Spectrograph (STIS) E140M data (PI: J. Linsky). COS is a slitless spectrograph with a diameter of $2''.5$, while the TW Hya data were taken through the $0''.5 \times 0''.5$ slit of STIS. The *HST*-COS data comprise mostly observations from the Disks, Accretion, and Outflows (DAO) of Tau guest observing program (PID 11616; PI: G. Herczeg), with a few targets from the COS Guaranteed Time Observing program (PID 11533 and 12036; PI: J. Green). The far-UV COS data were calibrated using the COS calibration program (CALCOS), then aligned and co-added using the procedure described in Danforth et al. (2010). Multiple central wavelengths and focal-plane positions were used to cover the wavelength range from ≈ 1150 – 1750 Å while minimizing fixed pattern noise.

3. H_2 FLUORESCENCE

H_2 fluorescence from protoplanetary disks can be used as a probe of the UV extinction curve along the line of sight toward these objects. The H_2 in the disk is pumped into electronically excited states by the stellar $\text{Ly}\alpha$ emission, and fluoresces as the electron returns to the ground electronic state, $X^1\Sigma_g^+$. This emission then travels through the interstellar and circumstellar media before being observed (see Figure 1). The interstellar and circumstellar media can absorb some of the fluorescent emission along the line of sight, causing us to see a weaker and redder H_2 fluorescence spectrum. Comparing this reduced spectrum with a model fluorescence spectrum will reveal the extinction curve as the difference between the two.

We study seven strong H_2 progressions $((v', J') = (0, 1), (0, 2), (1, 4), (1, 7), (4, 4), (2, 12), \text{ and } (3, 13))$ in the Lyman electronic band ($B^1\Sigma_u^+ - X^1\Sigma_g^+$). The progression lines arise from the H_2 in each (v', J') state of the excited $B^1\Sigma_u^+$ electronic state transitioning into many different (v'', J'') states of the ground electronic state. The branching ratios of the excited state determine the amount of flux distributed into each downward transition. We use reconstructed $\text{Ly}\alpha$ profiles from Schindhelm et al. (2012b) and France et al. (2014) to excite the H_2 molecules in our fluorescence model. These profiles are reconstructed using measured line fluxes from 12 H_2 progressions in the wavelength range 1395–1640 Å, where self-absorption is negligible. The total flux fluoresced from each progression is found by adding up the flux divided by the branching ratio for each line in the progression. These fluxes are divided by the equivalent width of the absorbing transition of each progression to get the flux incident on the H_2 at each

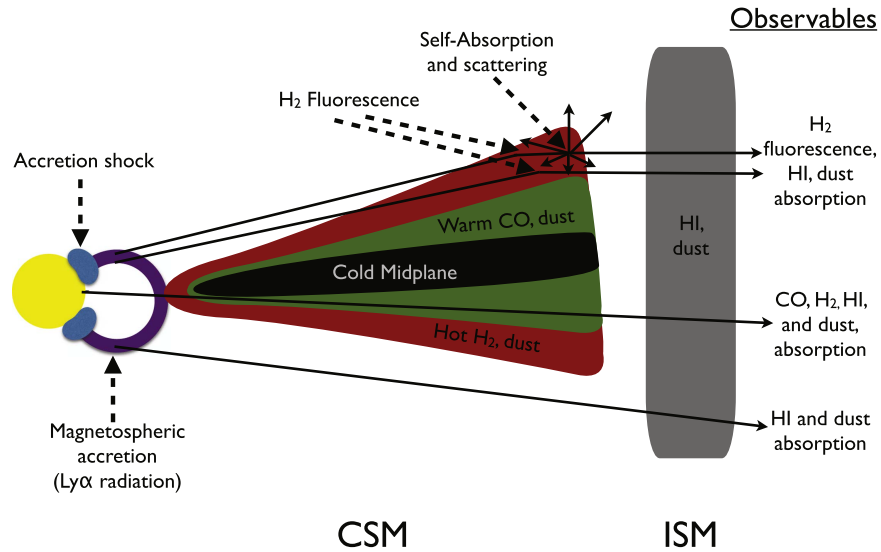


Figure 1. Sketch of some important observables along different lines of sight toward young stars. Different photon paths are the solid black lines, and the dotted black lines label important locations. The sketch is broken into circumstellar material (CSM) and interstellar material (ISM). The circumstellar material consists of the disk with components of a cold, unobservable, midplane, a warm middle layer with H_2 , CO, and dust, and a hot upper layer with H_2 , dust, and possibly H I. The interstellar material consists of interstellar dust and H I. Lines of sight that pass through the lower layers of the disk and upper layers of the disk are shown as well as a line of sight that avoids the disk entirely. Only one side of the disk is shown, though H_2 fluorescence measurements probe emission from both sides of the disk. The amount of emission and absorption observed for any given source depends on inclination and the degree of disk flaring. Observables are listed on the right.

progression wavelength. Model profiles that include H I absorption between the star and the H_2 are then fit to the 12 incident flux data points to determine the best-fit $\text{Ly}\alpha$ profile. We then use these reconstructed profiles to predict the flux at shorter wavelengths, compare the prediction to observed H_2 line fluxes, and estimate a UV extinction curve.

Calculating the $\text{Ly}\alpha$ profiles with this method used certain assumptions. These included: (1) H_2 that is isothermal, well mixed, co-spatial, and at rest with respect to the star, (2) a uniform filling fraction ($\eta = 1$), (3) the only opacity source between the stellar $\text{Ly}\alpha$ profile and the H_2 is H I, (4) the amount of H_2 that the $\text{Ly}\alpha$ travels into is the amount of H_2 that we observe, and (5) the entire $\text{Ly}\alpha$ profile reaches the H_2 in the disk equally. These assumptions are presented in more detail in the [Appendix](#). We discuss the impact of our reliance on the $\text{Ly}\alpha$ profiles of Schindhelm et al. (2012b) and France et al. (2014) in the next section.

H_2 self-absorption, however, can mimic the effects of extinction, and must be taken into account before comparing the model to the observations (Wood et al. 2002). The fluoresced photons from a $\text{Ly}\alpha$ -pumped H_2 molecule falling back down to the ground state can be reabsorbed by another H_2 molecule along the line of sight before the photons escape the disk. The photons are then fluoresced again, possibly out of the original line of sight, causing that flux to be lost. This flux loss mimics interstellar absorption, where interstellar dust absorbs and scatters flux out of the line of sight as photons move from the star toward our instrument. Self-absorption is stronger at shorter wavelengths since there is a larger molecular population in these lower rovibrational states. We can predict the amount of self-absorption that occurs in the disk by fitting the H_2 fluorescence lines at longer wavelengths ($\lambda > 1450 \text{ \AA}$, high v'' , J'' , where self-absorption is negligible) to derive a best-fit temperature and column density of H_2 molecules. These parameters then predict the amount of self-absorption based on the optical depth of H_2 in each absorbing level. The optical depths of the H_2 progressions for an average column density

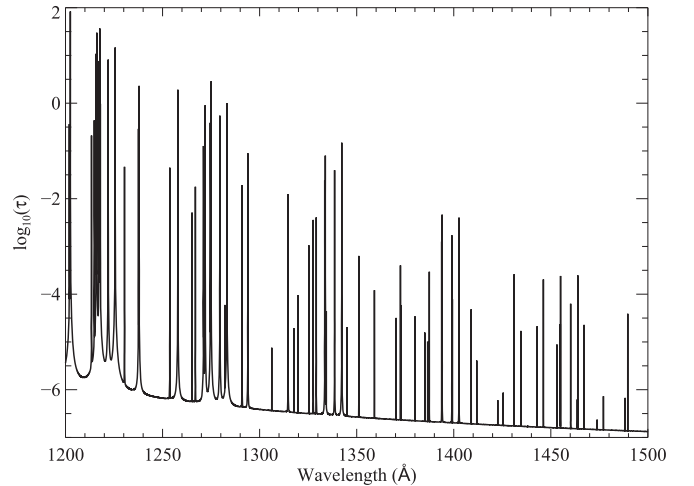


Figure 2. Plot of the logarithm of the optical depth as a function of wavelength for many of the far-UV H_2 lines. The optical depths assume $\log_{10}(N(\text{H}_2)) = 19.0$ and $T = 1500 \text{ K}$. The increasing low-level opacity toward shorter wavelengths comes from the broad Lorentzian wings of the $(v' - v) = (0-0)$ Lyman band absorption.

($\log_{10}(N(\text{H}_2)) = 19.0$) and temperature ($T = 1500 \text{ K}$) are shown in Figure 2. Our self-absorption cutoff of 1450 \AA corresponds roughly to $\tau < 10^{-4}$.

4. MODELS

4.1. $\lambda > 1450 \text{ \AA}$ Fits

To model the longer wavelength H_2 fluorescence lines, we used a directory of UV H_2 line properties from Abgrall et al. (1993a, 1993b) that contains laboratory wavelengths, upper and lower v and J values, band identifiers, Einstein A -values, and Γ values (see below) for 62,785 H_2 lines. We then calculated the oscillator strengths and branching ratios using

the equations

$$f_{lu} = \frac{m_e c}{8\pi^2 e^2} \frac{g_u}{g_l} \lambda_{lu}^2 A_{ul} \quad (1)$$

$$f_{ul} = \frac{g_l}{g_u} f_{lu} \quad (2)$$

$$r_{\text{branch}} = \frac{A_{ul}}{\sum A_{ul}} \quad (3)$$

where f_{lu} and f_{ul} are the oscillator strengths for absorption and emission, r_{branch} is the branching ratio, g_u and g_l are the degeneracies of the upper and lower states (equal to $2J_u + 1$ and $2J_l + 1$, respectively), and A_{ul} is the Einstein A-value. We used the reconstructed Ly α profiles of Schindhelm et al. (2012b) and France et al. (2014) as the pumping radiation and calculated the absorbing cross-sections of the H₂ molecules using

$$\sigma_{lu} = \frac{\sqrt{\pi} e^2}{m_e c b} f_{lu} \lambda_{lu} H(a, y) \quad (4)$$

where $H(a, y)$ is the Voigt function with

$$a = \frac{\Gamma}{4\pi\Delta\nu} \quad (5)$$

$$y = \frac{|\nu - \nu_0|}{\Delta\nu} \quad (6)$$

$$\Delta\nu = \frac{b}{c} \nu. \quad (7)$$

The Γ parameter is listed for each line in the directory of Abgrall et al. (1993a, 1993b) and is the inverse of the mean lifetime of the upper level. The y parameter takes into account shifts in the frequency of the line due to shifts in velocity, and the b parameter is the Doppler b -value.

We thermally populated the H₂ molecular energy levels, with each (v, J) level having a column density of

$$N(v, J) = N_{\text{tot}} \frac{(2J + 1)(2s + 1)e^{-E(v, J)/k_b T}}{\sum_{v, J} (2J + 1)(2s + 1)e^{-E(v, J)/k_b T}} \quad (8)$$

where s is the nuclear spin (0 for even J values, 1 for odd J values), $E(v, J)$ is the energy in each (v, J) state, N_{tot} is the total column density in all states, and k_b is the Boltzmann constant. The ground-state energies are defined by

$$\begin{aligned} E(v, J) &= G(v) + F_v(J) \\ &= \omega_e \left(v + \frac{1}{2} \right) - \omega_e x_e \left(v + \frac{1}{2} \right)^2 + \dots \\ &\quad + B_v J(J + 1) - D_v J^2(J + 1)^2 + \dots \end{aligned} \quad (9)$$

where G_v represents the energy from the vibrational state v , and $F_v(J)$ represents the energy from the rotation in a given vibrational level. ω_e , x_e , B_v , and D_v are measured constants (Herzberg 1950).

The optical depth in each absorption line is the combination of the absorbing cross-section and the column density in each line:

$$\tau = N(v, J) \sigma_{lu}. \quad (11)$$

However, as some absorption lines overlap, we must correct the optical depths so that the lines do not overabsorb the available Ly α flux. The flux is shared between adjacent

absorbing transitions using the formula for the corrected optical depth (Liu & Dalgarno 1996; Wolven et al. 1997):

$$\tau_{\text{corr}} = \tau \frac{\tau}{\sum \tau} \quad (12)$$

where we sum over the optical depths of all the lines sharing the wavelength space.

The amount of flux absorbed by each absorbing transition is then

$$F_{\text{abs}} = \int (1 - e^{-\tau_{\text{corr}}}) F_{\text{Ly}\alpha} \quad (\text{erg cm}^{-2} \text{ s}^{-1}) \quad (13)$$

where $F_{\text{Ly}\alpha}$ is the reconstructed Ly α flux profile that we integrate over the full Ly α line. This flux is then stored in an array of excited states labeled by the v' and J' values. The model absorption of the H₂ against the Ly α flux is shown in the left plot of Figure 3 for TW Hya. Warm H₂ absorption superimposed on the Ly α emission spectra has been observed in DF Tau, V4046 Sgr, and AA Tau (Yang et al. 2011; France et al. 2012a). The right plot of Figure 3 shows the procedure for the optical depth correction for overlapping lines. The flux in the excited states is redistributed into the H₂ fluorescent lines. Each fluorescent line of a particular excited state is assigned a flux equal to the branching ratio of that state multiplied by the flux in the excited state. The absorbed flux is thus completely redistributed into the H₂ fluorescence.

We compared the flux (in $\text{erg cm}^{-2} \text{ s}^{-1}$) in the model lines to the flux in the matching line in the data focusing on our seven strong progressions: $(v', J') = (0, 1), (0, 2), (1, 4), (1, 7), (4, 4), (2, 12),$ and $(3, 13)$. We measured the data line fluxes using the interactive multi-Gaussian line-fitting code of France et al. (2012b). The code fits the background flux with a second-order polynomial, and fits the H₂ emission with a Gaussian line shape convolved with the COS line-spread function. For the TW Hya STIS data, unconvolved Gaussians were used for the H₂ line fits. We checked the data and removed lines that were blended, had low signal-to-noise ratio, or were badly fit by the H₂ line-fitting code. This means that not every target has the same number of studied lines as other targets, and that certain wavelength regions may be less populated for some targets. We searched over a grid of logarithmic column densities ranging from 17.5 to 22.5 dex in increments of 0.1 dex, and a grid of temperatures ranging from 500 to 3500 K in increments of 100 K. The fit of column density had to be extended down to $\log_{10}(N(\text{H}_2)) = 15.0$ for DR Tau, which was found to have a very low column density of $\log_{10}(N(\text{H}_2)) = 15.2$. We only compared the flux in the model and data lines. Line shapes were not important for the total flux comparison and were not calculated in the present model (see Hoadley et al. 2015 for a detailed H₂ line shape analysis).

To assess the impact of our reliance on the Ly α profiles of Schindhelm et al. (2012b) and France et al. (2014), we performed a grid search to determine the best-fit absorbed flux to the data. We took a grid of 0%–200% of the absorbed flux in our Ly α -pumped model (F_{abs}) for each progression, with steps of 10%. We then calculated the resulting flux in each H₂ emission line with the branching ratios as before. For most of the progressions of each target, we find best-fit absorbed flux values within 30% of the flux absorbed from the Ly α profiles of Schindhelm et al. (2012b) and France et al. (2014). Only the (4, 4) progression of some targets is outside of this range, sometimes needing $\sim 50\%$ more absorbed flux into the

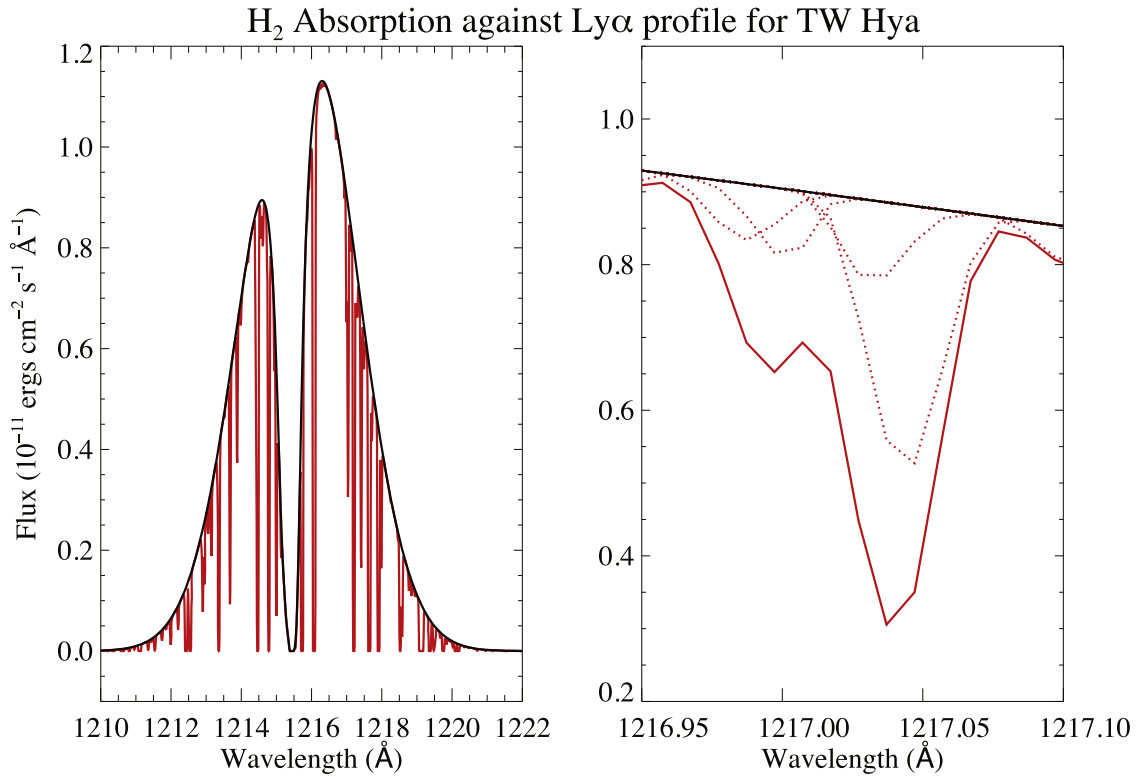


Figure 3. Plot showing the H_2 absorption against the pumping $\text{Ly}\alpha$ radiation. Left: full wavelength figure of the pumping $\text{Ly}\alpha$ profile in black and the absorbed profile in red. Right: an enlargement of the absorption against the $\text{Ly}\alpha$ profile showing four absorption lines (dotted lines) sharing the optical depth space. The four lines combine to create the solid red absorption line.

progression to explain the fluoresced flux. We hope to better understand this anomalous progression in future work by modeling each progression with a different H_2 column density and temperature (see Section 6).

The best-fit temperatures and column densities from the fluorescence flux fits are listed in Table 1. Figure 4 shows the ratio of the data line fluxes over the model line fluxes for RECX-11. The flux difference is a factor of 8.1 at $\lambda \sim 1180$ Å, a factor of 2.0 at $\lambda \sim 1280$ Å, and a factor of 1.1 at $\lambda \sim 1380$ Å. The strong wavelength dependence of the model/observed flux ratio is the result of the combined effects of self-absorption and dust attenuation.

4.2. Calculation of Self-absorption

In the case of an optically thick H_2 population, light previously fluoresced by H_2 molecules can be reabsorbed by nearby H_2 and subsequently scattered out of the line of sight. Self-absorption preferentially occurs at shorter wavelengths where the energy levels are well populated. Attenuation due to dust extinction also increases with decreasing wavelength. This process can thus be confused with extinction and must be corrected for in our calculations. To correctly account for self-absorption, a full radiative transfer calculation should be used. This involves taking into account velocity broadening (including thermal and turbulent broadening along with potential line-of-sight velocities due to disk winds) as well as geometric effects (such as the clumping and density gradients of the disk material). The thermal and turbulent velocities are treated by including a physically motivated Doppler b -value in our model. We calculated a range of b -values assuming that the turbulent velocity was $\lesssim 1.0 \text{ km s}^{-1}$

Table 1
 H_2 Model Best-fit Parameters

Object	$\log_{10}(N(\text{H}_2))$	T (K)
AA Tau	$20.0^{+0.3}_{-0.4}$	1000^{+800}_{-200}
BP Tau	$18.1^{+0.2}_{-0.4}$	1600^{+500}_{-300}
DE Tau	$18.0^{+1.1}_{-1.4}$	1700^{+1100}_{-600}
DF Tau	$18.1^{+0.2}_{-0.3}$	1300^{+600}_{-200}
DM Tau	$22.0^{+0.4}_{-0.7}$	1200^{+700}_{-200}
DR Tau	$15.1^{+0.4}_{-0.7}$	1500^{+200}_{-300}
GM Aur	$20.0^{+0.5}_{-0.7}$	1500^{+1100}_{-200}
HN Tau	$20.1^{+0.3}_{-0.3}$	1000^{+800}_{-200}
LkCa15	$18.0^{+0.3}_{-0.6}$	1500^{+500}_{-300}
RECX-11	$18.1^{+0.2}_{-0.1}$	1800^{+600}_{-300}
RECX-15	$20.1^{+0.4}_{-0.5}$	1400^{+800}_{-200}
RU Lupi	$18.0^{+0.2}_{-1.4}$	1800^{+800}_{-600}
SU Aur	$18.5^{+0.2}_{-0.3}$	1200^{+500}_{-200}
TW Hya	$19.0^{+0.8}_{-1.0}$	2500^{+1000}_{-800}
UX Tau	$21.0^{+0.6}_{-0.6}$	1000^{+700}_{-200}
V4046 Sgr	$19.5^{+0.5}_{-0.5}$	1700^{+600}_{-200}
Avg.	19.0	1500

and that the H_2 rotational temperature was $\lesssim 5 \times 10^3$ K. The b -values ranged from 0.0 to 3.0 km s^{-1} , of which we chose 1.5 km s^{-1} as a representative value. There is evidence of disk winds (e.g., Pontoppidan et al. 2011; Schneider et al. 2013), which are largely perpendicular to the disk, so we therefore neglect the offsets in radial velocity with respect to the stellar $\text{Ly}\alpha$. As mentioned in Section 3, because the $\text{Ly}\alpha$ profiles are very broad, even H_2 molecules in winds that are not

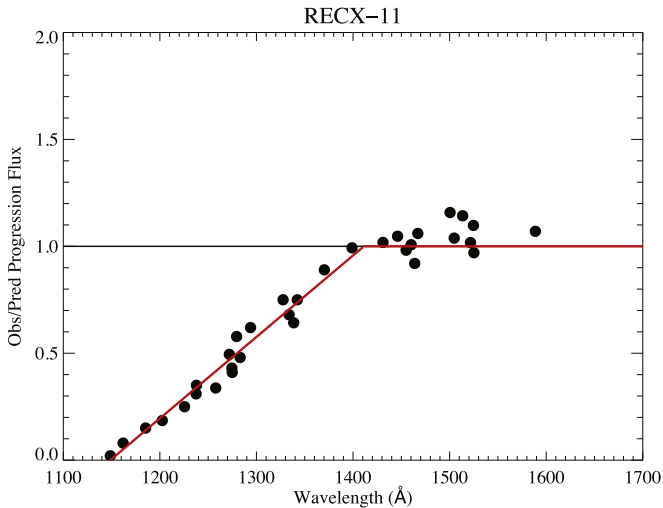


Figure 4. Plot of the data H_2 line fluxes divided by the model H_2 line fluxes for RECX-11 before the self-absorption correction. A fit to the falloff at short wavelengths is shown as a linear function overplotted in red for display.

perpendicular to the disk with velocities of $\sim 20 \text{ km s}^{-1}$ have negligible impact on the amount of $\text{Ly}\alpha$ flux absorbed for most targets. The density distribution of the disk gas, however, is currently not well known in disk models. Without an approximation of the expected clumpiness, the calculation is prohibitively computationally expensive. To simulate the effect of self-absorption without knowing the density distribution of disk gas, we used the best-fit temperature and column density of the H_2 fluorescence lines to calculate the optical depth (Equations (11) and (12)) of each transition. The transmission is a direct measure of the total self-absorption, so that dividing the observed/predicted plot points in Figure 4 by the corresponding line transmission gives the self-absorption-corrected curve. We plot the self-absorption-corrected curves for all 16 targets as black points in Figures 5(a) and (b) with the extinction curve fit overplotted in blue.

4.3. Extinction Curve Fits

We found the best-fit UV extinction curve by comparing our self-absorption-corrected curves to extinction curves of Cardelli et al. (1989) for a grid of A_V and R_V values. We took A_V values in the range from 0 to 2 in steps of 0.1. Higher extinction values correspond to larger interstellar H I values through the relation of Bohlin et al. (1978): $N(\text{H I})/E(B - V) = 4.8 \times 10^{21} \text{ atoms cm}^{-2} \text{ mag}^{-1}$ because $E(B - V) = A_V/R_V$. We set $A_V = 2$ as the upper limit because for $A_V = 2$ and $R_V = 3.1$, $N(\text{H I}) = 3.1 \times 10^{21} \text{ atoms cm}^{-2}$, which would lead to a $\text{Ly}\alpha$ profile completely absorbed by interstellar H I (France et al. 2012a; McJunkin et al. 2014). The R_V values ranged from 2 to 6 in steps of 0.1 based on the spread of well-determined literature R_V values ($R_V = 2.1$ for HD 210121 (Welty & Fowler 1992) to $R_V \approx 5.7$ for HD 36982 (Cardelli et al. 1989; Fitzpatrick 1999)). The minimum χ^2 value between the models and the data was chosen as the best-fit extinction model. The extinction curve fits are plotted in blue in Figures 5(a) and (b).

5. RESULTS

5.1. Best-fit Models and Parameters

The best-fit H_2 column densities and temperatures are listed in Table 1. The column densities range from approximately $\log_{10}(N(\text{H}_2)) = 18.0$ to $\log_{10}(N(\text{H}_2)) = 20.0$, while the temperatures are centered around $T = 1500 \text{ K}$ with large errors. Within the large errors, our targets are all at roughly the same temperature. The error bars for each parameter were calculated by increasing (or decreasing) the parameter from the best-fit value, keeping other parameters constant, and finding the point where the χ^2 value increased by one. Within the error bars, our temperatures are consistent with those found in the H_2 radiative transfer model of Hoadley et al. (2015) for all targets except AA Tau. Previous H_2 line studies (Ardila et al. 2002; Herczeg et al. 2004; France et al. 2012a; Hoadley et al. 2015) have also found temperatures for these types of targets in the range 1000–4000 K. It is difficult to constrain the temperatures tightly because one needs to measure the weaker, higher- J lines, which often blend into the noise of the data.

The best-fit extinction curves for the targets can be seen in Figure 5 and the best-fit $A_V(\text{H}_2)$ and R_V values for all the targets are listed in Table 2. Black points in Figure 5 are the points corrected for self-absorption, while the gray points are the data before the self-absorption correction. Some targets have extinction curves with shapes that are not well fit by a curve of Cardelli et al. (1989) (defined in Section 5.2). This hints that grain processing is occurring in the vicinity of the disk and that the disk is contributing significantly to the extinction. The ISM and disk likely have different R_V values, possibly leading to the poor single- R_V fits. The circumstellar material that we are probing is most likely material outside the location of the fluorescence. Hoadley et al. (2015) find outer limits of the H_2 fluorescence radii (r_{out, H_2}) that range between 0.87 and 12.03 AU for our overlapping targets. Dust inside the H_2 fluorescence radii is not appreciable if we assume an interstellar dust-to-gas ratio as well as an upper limit on the $N(\text{H I})$ between the star and the H_2 fluorescence radii from Schindhelm et al. (2012a). They find that the $N(\text{H I})$ between the star and the fluorescent CO disk surface is $\log_{10}(N(\text{H I})) \sim 19\text{--}20$ (Schindhelm et al. 2012a, Table 5). The amount of $N(\text{H I})$ between the star and the H_2 , which lies closer to the star, is necessarily larger. The dust-to-gas ratio would need to be ~ 100 times the interstellar value to have appreciable dust in this region.

5.2. Model and Parameter Analysis

Targets with good extinction fits, defined as those with reduced χ^2 values between 0.75 and 1.25, are listed in Table 3 with $A_V(\text{H}_2)$ values from this work as well as values from previous works. The literature extinctions in the table utilize methods in four different wavelength regions: IR, UV, optical, and X-ray. For clarity, extinctions derived from the IR and X-ray measurements are designated as $A_V(\text{IR})$ and $A_V(\text{X-ray})$ respectively, with the UV method of McJunkin et al. (2014) designated as $A_V(N(\text{H I}))$, and the optical method of Herczeg & Hillenbrand (2014) designated as $A_V(\text{SED})$. Furlan et al. (2011) derive IR extinction values using Two Micron All Sky Survey magnitudes, assumed $J - H$ or $J - K$ photospheric colors, and a standard interstellar reddening law. McJunkin et al. (2014) use interstellar H I absorption against the stellar $\text{Ly}\alpha$ profile to measure $N(\text{H I})$ and derive visual extinctions assuming standard interstellar gas-to-dust ratios. Herczeg & Hillenbrand (2014)

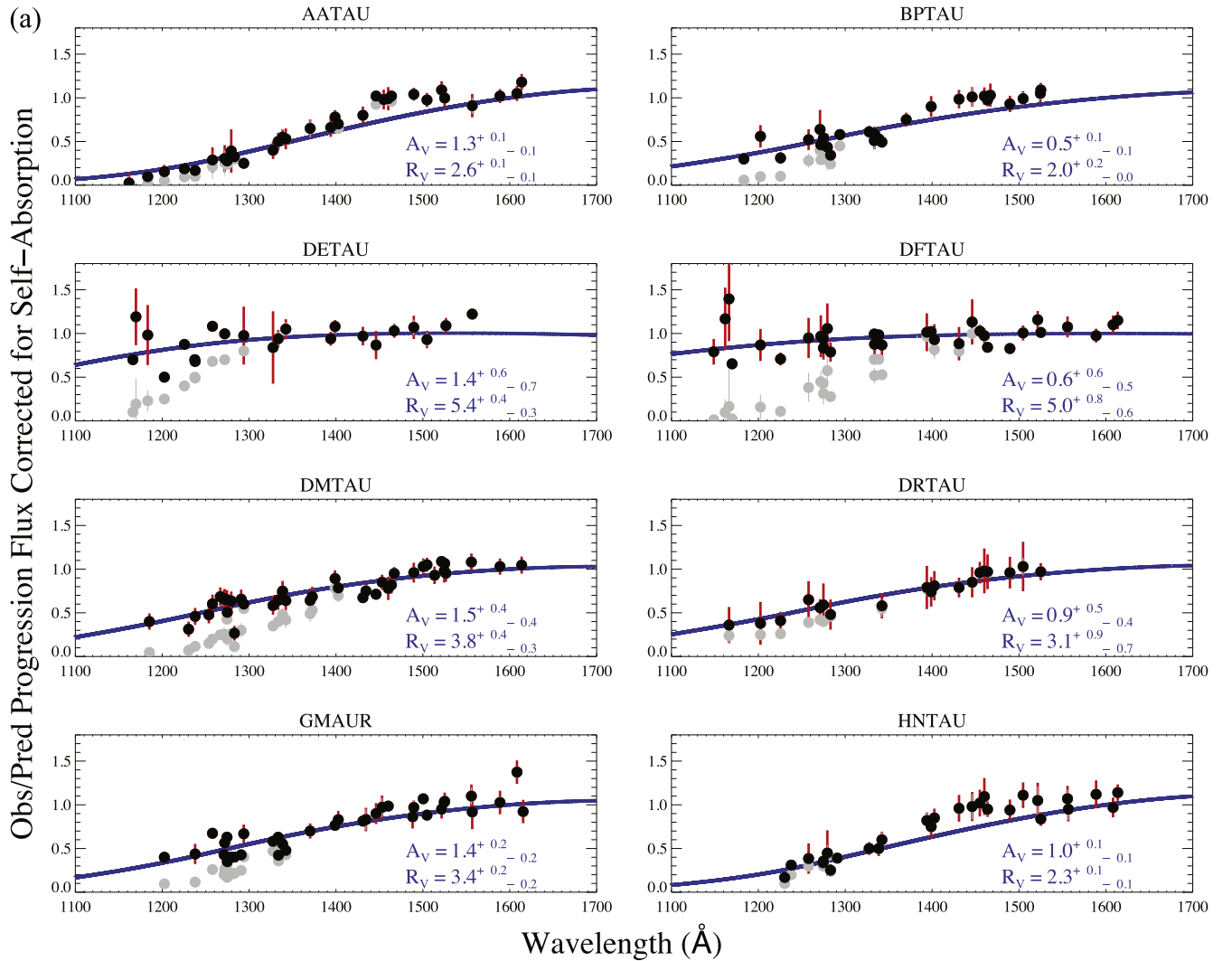


Figure 5. (a) Far-UV extinction curve fits for the first half of the targets. The black points are corrected for self-absorption, the gray points are before the self-absorption correction, and the blue line is the extinction curve. Errors on the black points are shown in red, while the gray points also have gray errors. Some error bars are smaller than the data points. Extinctions of $A_V(H_2) = 2.0$ represent the numerical upper limit of our parameter searches. Targets such as V4046 Sgr and TW Hya have extinction fits with large $A_V(H_2)$ values, but the scatter in the V4046 Sgr data points is consistent with an extinction of zero, and the lack of lines in TW Hya at the shortest wavelengths fails to constrain the extinction well. (b) Same as part (a) for the second half of the targets.

obtain visual extinction values using weak-line photospheric templates of T Tauri stars and an accretion continuum fit to broadband optical spectra. The X-ray extinction method uses two-temperature fits to spectra of CCD resolution ($R \sim 15\text{--}20$) to obtain H I column densities, which are converted to $A_V(X\text{-ray})$ values similarly to McJunkin et al. (2014). The $A_V(H_2)$ values derived in this work for AA Tau, GM Aur, and RECX-11 are inconsistent with all previous literature values, while the other targets are inconsistent with some literature values and consistent with others.

V4046 Sgr and TW Hya have A_V values that are consistent with the low A_V expected from previous studies (e.g., 0.04 mag (McJunkin et al. 2014) and 0.19 mag (Argiroffi et al. 2012) for V4046, and 0.04 mag (McJunkin et al. 2014) and 0.13 mag (Stelzer & Schmitt 2004) for TW Hya) and their relative proximity to the Sun, though with their large error bars we do not constrain the A_V values of the two targets. The large errors are likely due to the large scatter in the data points at shorter wavelengths for V4046 Sgr and the lack of data points at shorter wavelengths for TW Hya. V4046 Sgr and TW Hya are

nearby stars with distances of 73 pc (Torres et al. 2008) and 54 pc (van Leeuwen 2007) respectively. Bohlin et al. (1978) find that stars with distances less than 100 pc have color excesses $E(B - V) \ll 0.1$ mag, or $A_V \ll 0.3$ mag assuming $R_V = 3.1$.

BP Tau and DE Tau have very similar H_2 column densities and temperatures, but quite different A_V and R_V values. This difference is driven by the observed flux ratios between the lines of higher and lower wavelength. The ratio of the higher wavelength lines to the lower wavelength lines of BP Tau is larger than that of DE Tau. The ratio also starts increasing at a higher wavelength in BP Tau (1400 Å) than in DE Tau (1300 Å), leading to different shapes of the extinction curves. DE Tau has a much shallower turnoff at lower wavelengths than BP Tau. This can be described in two different ways, because A_V and R_V are not independent in creating an extinction curve. The shallower curve of DE Tau can be described by a larger R_V value indicative of gray extinction, or a smaller A_V value. For better comparison with previous literature extinction values, we made a second extinction curve fit in which we set

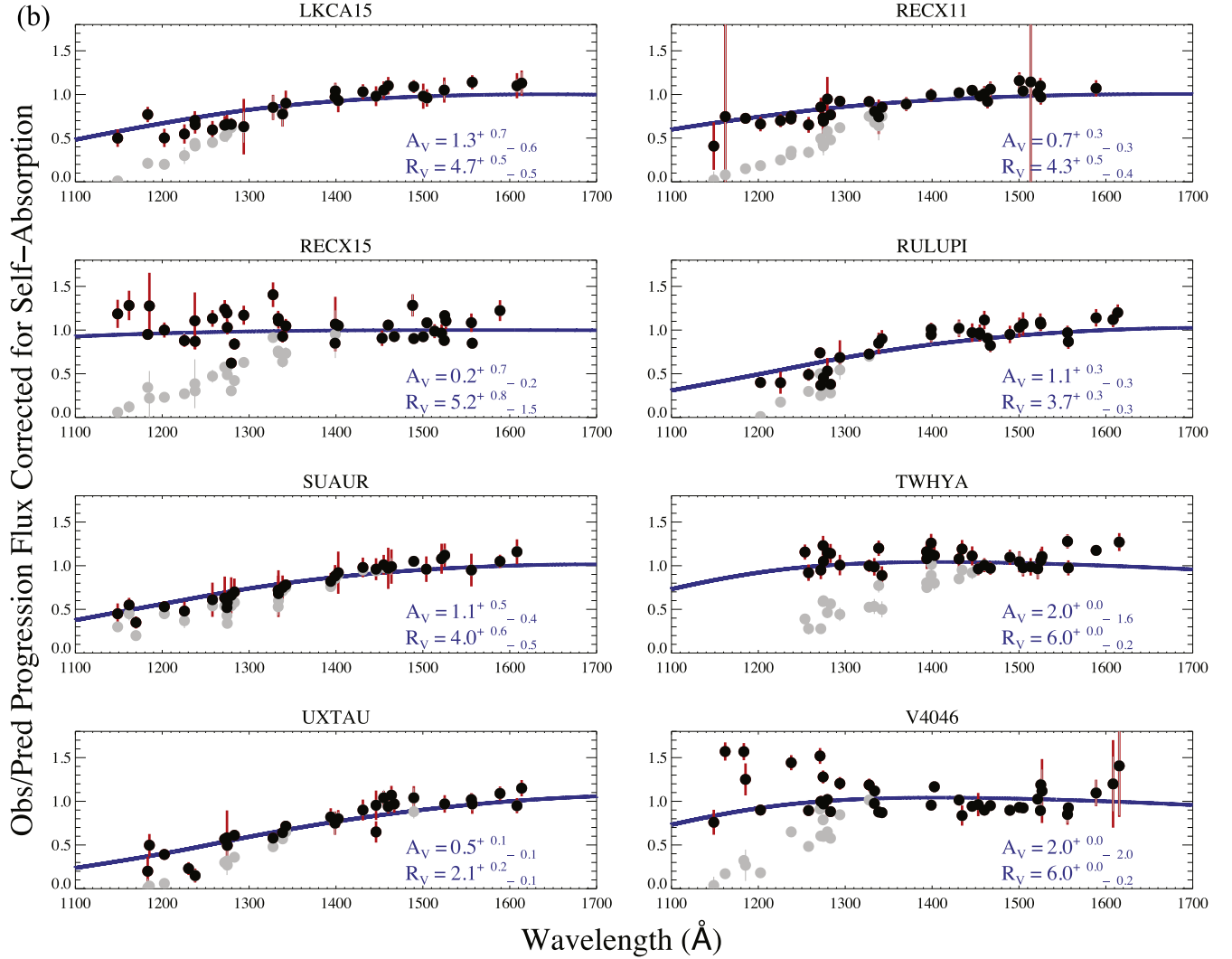


Figure 5. (Continued.)

$R_V = 3.1$ and let only the A_V value vary. The results are listed in the rightmost column of Table 2. Some targets, such as RECX-11, TW Hya, and V4046 Sgr, have best-fit extinctions consistent with previous literature values with the new fit, though others, such as AA Tau, BP Tau, and HN Tau, have best-fit values more inconsistent with literature values than our previous fit.

RECX-11 and RECX-15 are quoted in the literature as having zero extinction from measurements of optical colors (Luhman & Steeghs 2004). We find that RECX-15 is consistent with zero extinction ($A_V(\text{H}_2) = 0.2^{+0.7}_{-0.2}$ mag) but RECX-11 is not ($A_V(\text{H}_2) = 0.7^{+0.3}_{-0.3}$ mag). RECX-15 has a bit of scatter in the data-to-model H_2 line fluxes at short wavelengths, similar to V4046 Sgr and TW Hya, so that even though the fit finds an extinction of 0.2 mag, $A_V(\text{H}_2) = 0$ mag (a horizontal line) also fits the data. RECX-11 has a noticeable turnover in the data at shorter wavelengths and is not well fit by a curve of $A_V(\text{H}_2) = 0$ mag. Inclination and disk flaring could play a role in this discrepancy between the two η Cha stars because the fluorescing H_2 is primarily in the upper atmosphere of the disk. However, Lawson et al. (2004) find inclinations of 70° and 60° for RECX-11 and RECX-15, respectively. The stars have

little difference in published inclination, though these inclinations are derived from $\text{H}\alpha$ profile fits, which are less accurate than inclinations for other targets in the literature (McJunkin et al. 2014).

5.3. Predicted NUV Bump at 2175 Å

Future work with NUV data for these sources can search for the 2175 Å bump feature. If a bump is observed, it indicates that there is still a significant population of small grains in the star-forming cloud. We extend the best-fit extinction curves from Figure 5 to longer wavelengths in Figure 6 in order to see the predicted 2175 Å bump, which is very pronounced for some targets. However, the predicted 2175 Å bump is not very pronounced in DM Tau or LkCa15. For these targets as well as others in our sample, the weak 2175 Å bump is similar to the anomalous extinction laws of HD 29647 and HD 283809 in Calvet et al. (2004). Most of the errors on the points in the plot are too small to see in the figure. Verification of the presence of a visible 2175 Å bump in these targets would allow us to independently assess the contribution of small grains in the circumstellar and star-forming cloud environments.

Table 2
Extinction Model Best-fit Parameters

Object	$A_V(H_2)$	R_V	$A_V(H_2) (R_V = 3.1)^a$
AA Tau	$1.3^{+0.1}_{-0.1}$	$2.6^{+0.1}_{-0.1}$	$1.8^{+0.2}_{-0.1}$
BP Tau	$0.5^{+0.1}_{-0.1}$	$2.0^{+0.2}_{-0.0}$	$1.1^{+0.1}_{-0.2}$
DE Tau	$0.8^{+0.3}_{-0.3}$	$4.5^{+0.5}_{-0.4}$	$0.3^{+0.1}_{-0.2}$
DF Tau	$0.3^{+0.3}_{-0.3}$	$4.3^{+1.2}_{-0.8}$	$0.1^{+0.2}_{-0.1}$
DM Tau	$1.5^{+0.4}_{-0.4}$	$3.8^{+0.4}_{-0.3}$	$0.9^{+0.3}_{-0.2}$
DR Tau	$0.9^{+0.5}_{-0.4}$	$3.1^{+0.9}_{-0.7}$	$0.9^{+0.5}_{-0.4}$
GM Aur	$1.4^{+0.2}_{-0.2}$	$3.4^{+0.2}_{-0.2}$	$1.1^{+0.2}_{-0.1}$
HN Tau	$1.0^{+0.1}_{-0.1}$	$2.3^{+0.1}_{-0.1}$	$1.7^{+0.2}_{-0.1}$
LkCa15	$1.3^{+0.7}_{-0.6}$	$4.7^{+0.5}_{-0.5}$	$0.4^{+0.2}_{-0.2}$
RECX-11	$0.7^{+0.3}_{-0.3}$	$4.3^{+0.5}_{-0.4}$	$0.3^{+0.1}_{-0.2}$
RECX-15	$0.2^{+0.7}_{-0.2}$	$5.2^{+0.8}_{-1.5}$	$0.0^{+0.2}_{-0.0}$
RU Lupi	$1.1^{+0.3}_{-0.3}$	$3.7^{+0.3}_{-0.3}$	$0.7^{+0.2}_{-0.2}$
SU Aur	$1.1^{+0.5}_{-0.4}$	$4.0^{+0.6}_{-0.5}$	$0.6^{+0.3}_{-0.3}$
TW Hya	$2.0^{+0.0}_{-1.6}$	$6.0^{+0.0}_{-0.2}$	$0.0^{+0.1}_{-0.0}$
UX Tau	$0.5^{+0.1}_{-0.1}$	$2.1^{+0.2}_{-0.1}$	$1.0^{+0.2}_{-0.1}$
V4046 Sgr	$2.0^{+0.0}_{-2.0}$	$6.0^{+0.0}_{-0.2}$	$0.0^{+0.1}_{-0.0}$

Note.

^a Best-fit $A_V(H_2)$ values from our modeling of the extinction curve assuming $R_V = 3.1$.

Table 3
 A_V Comparison for Best-fit Targets

Object	$A_V(H_2)$	$A_V(N(H\ I))$	$A_V(IR)$	$A_V(SED)$	$A_V(X-ray)$
	(this work)	McJunkin et al. (2014)	Furlan et al. (2011)		
AA Tau	$1.3^{+0.1}_{-0.1}$	0.34	1.95	0.40 ^a	6.07 ^b
BP Tau	$0.5^{+0.1}_{-0.1}$	0.17	1.06	0.45 ^a	0.58 ^b
DE Tau	$0.8^{+0.3}_{-0.3}$	0.31	0.89	0.35 ^a	...
DF Tau	$0.3^{+0.3}_{-0.3}$	0.54	1.95	0.10 ^a	...
GM Aur	$1.4^{+0.2}_{-0.2}$	0.51	0.57	0.30 ^a	2.97 ^c
HN Tau	$1.0^{+0.1}_{-0.1}$	0.36	1.06	1.15 ^a	1.29 ^b
LkCa15	$1.3^{+0.7}_{-0.6}$	0.31	1.06	0.30 ^a	2.39 ^d
RECX-11	$0.7^{+0.3}_{-0.3}$	0.03	...	0.0 ^c	0.04 ^f
RU Lupi	$1.1^{+0.3}_{-0.3}$	0.07	...	0.25 ^g	1.16 ^h
UX Tau	$0.5^{+0.1}_{-0.1}$	0.51	0.46	...	0.39 ^c

Notes.

^a Herczeg & Hillenbrand (2014).

^b Güdel et al. (2007).

^c X-ray data analyzed in McJunkin et al. (2014).

^d Skinner & Güdel (2013).

^e Testa et al. (2008).

^f López-Santiago et al. (2010).

^g DAO STIS G430L analyzed in McJunkin et al. (2014).

^h Robrade & Schmitt (2007).

6. DISCUSSION

While the majority of our targets are uncontaminated sources, a few have been shown to have strong outflows that may affect the H_2 line profiles. Using COS observations, France et al. (2012b) find that DF Tau, HN Tau, LkCa15, RECX-15, and RU Lup have H_2 emission with extended blue wings, possibly indicating an origin in an outflow component. However, LkCa15 and RU Lup had weaker extended emission and were adequately fit with a single Gaussian emission line, implying a disk origin. Using STIS spectra, Herczeg et al.

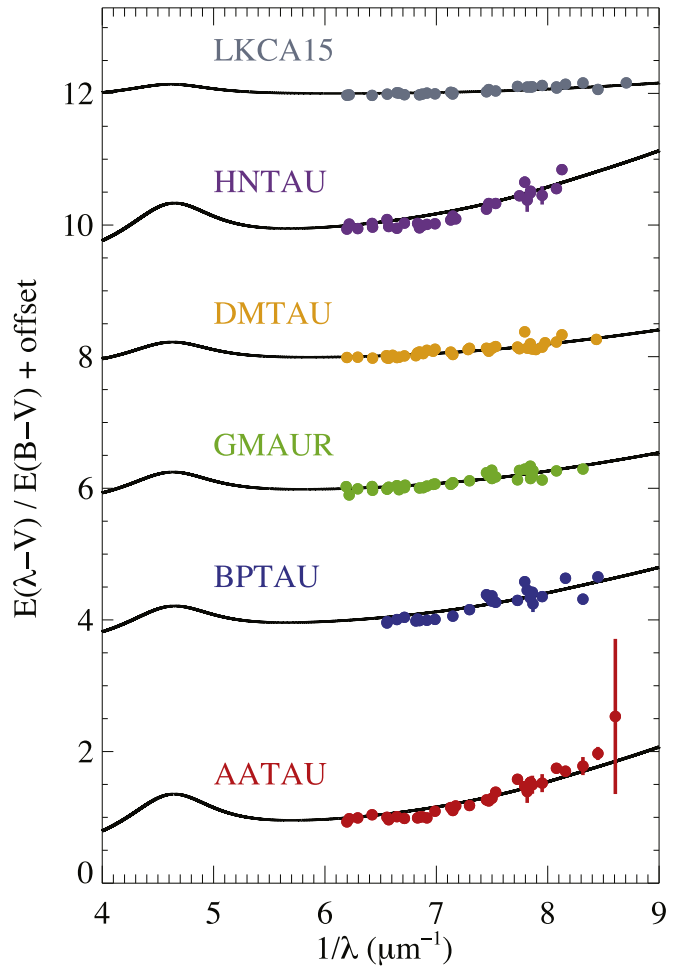


Figure 6. Extinction curves for six targets with noticeable extinction compared to their best-fit extinction curve of Cardelli et al. (1989). All of these targets predict noticeable dips in the transmission curve against the linear UV “continuum” fit, which we hope to observe in future observations. Observing a 2175 Å bump will indicate the presence of a population of small grains.

(2005, 2006) find that all of the H_2 fluorescence of RU Lup is contained in outflows. The difference between the COS and STIS data is puzzling, possibly indicating a time-dependent outflow or geometrical changes between observations (France et al. 2012b).

In our model fits, we assume a single H_2 column density and temperature for all progressions. This simplification works for the majority of our progressions, though we do see that for some of our targets the (4, 4) progression is not well fit by the best-fit model. This progression may absorb at a different location in the disk, better described by a separate temperature and column density, or may be the result of non-thermal excitation processes (e.g., France et al. 2012a). In the future, modifying the model to include a different column density and temperature value for each progression may lead to better line fits and a better understanding of the location of the fluorescence of each progression.

Little agreement exists between previous extinction studies in the literature over different wavelength ranges, and the $A_V(H_2)$ values found in this work are also quite disparate from the optical, H I, IR, and X-ray data (see Table 3). While all these methods traverse the same path through the ISM, they likely travel different paths through the circumstellar medium.

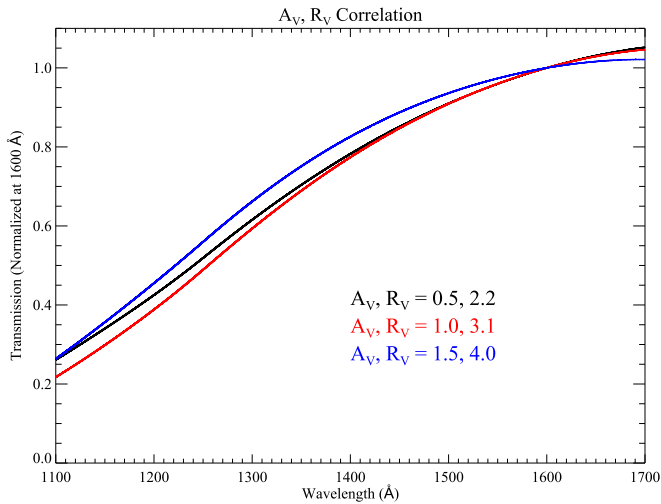


Figure 7. Three extinction curves for different pairs of (A_V, R_V) values. The black line is (0.5, 2.2), the red line is (1.0, 3.1), and the blue line is (1.5, 4.0). A_V and R_V are strongly correlated, so that a unique (A_V, R_V) extinction curve is difficult to determine without having a good estimate of either value. We present A_V values assuming a typical $R_V = 3.1$ value in Table 2 in order to break the degeneracy and for better comparison with the literature, which often assumes this R_V value in extinction calculations.

These different paths sample different areas of the disk, so it is not particularly surprising that the extinctions derived from different wavelength bands do not agree. Many of these CTTs are also variable, which may be caused by varying circumstellar obscuration (Herbst et al. 1994). Alencar et al. (2010) saw very prevalent variability in light curves of CTTs in NGC 2264 with *CoRoT*, possibly due to variable disk extinction from an inner disk warp. Cody et al. (2013) observed brightness fluctuations of 1%–10% over time periods of hours to weeks in CTTs in the Taurus–Auriga star-forming region. This stellar variability could be contributing to the different A_V values found in the literature for our targets.

The $A_V(H_2)$ values we obtain in this paper are generally higher than the $A_V(N(HI))$ values found in McJunkin et al. (2014) using interstellar H I absorption against the Ly α line. The H_2 method contains circumstellar extinction, whereas the H I method does not, which most likely contributes significantly to the difference in A_V . Many of the targets with higher $A_V(H_2)$ values have R_V values that differ from the typical interstellar value of 3.1, which is assumed in the calculation of the extinction in McJunkin et al. (2014). Changing the R_V value of the extinction curve directly affects the $A_V(H_2)$ value found for the extinction fit, possibly contributing to the differences in A_V between the two studies. R_V and A_V are strongly correlated: either increasing the A_V value or decreasing the R_V value leads to faster, deeper falloffs of the extinction curve at shorter wavelengths. Almost any extinction curve with a given R_V value can find an A_V value that creates a similar shape to another extinction curve with different A_V and R_V values (see, e.g., Fitzpatrick & Massa 2007). Similar extinction curves are created by the (A_V, R_V) pairs of (0.5, 2.2), (1.0, 3.1), and (1.5, 4.0). These three curves are plotted in Figure 7. This degeneracy can be broken by assuming a value for either A_V or R_V that is physically motivated or based on previous measurements, which we do by setting $R_V = 3.1$ in Section 5.2. For now, requiring A_V or R_V to be calculated independently may be a limitation of our new technique, which we hope to improve upon in future iterations. Using the calculated A_V

values, the predicted transmission at 1400 Å differs between this work and the study of McJunkin et al. (2014) by $\lesssim 0.15$ for most targets. This is about the average size of the error bars on the points of the extinction curve in this work (see Figure 5). The outliers are AA Tau, BP Tau, and LkCa15. Thus, the predicted extinctions are not vastly different for most targets even though the A_V values differ, because the R_V value is allowed to change.

R_V values greater than the canonical interstellar value of 3.1 indicate a dust grain population with relatively more larger grains and fewer smaller grains (Draine 2003). Conversely, R_V values less than 3.1 may indicate a dust grain population with more smaller grains and fewer larger grains. An enhanced population of small grains, seen in some of our targets with $R_V < 3.1$, is the opposite of what we would expect if grain growth were occurring in the star-forming region. We directly probe the upper layers of the disk with the H_2 fluorescence, so the larger grains may be settling toward the disk midplane faster than smaller grains, artificially increasing the fraction of small grains to large grains. Turbulence in the disk could also be breaking up larger grains and resupplying the population of small grains (Birnstiel et al. 2012).

This apparent evolution of grains could also result in non-LTE H_2 level populations as photoelectric heating of grains becomes less efficient, dropping the gas temperature at the disk surface (Nomura et al. 2007). France et al. (2012a) also find evidence for non-thermal H_2 level populations in AA Tau at high excitation temperatures. They find an increased population at high- J levels (excitation temperatures $> 2 \times 10^4$ K), suggesting that non-equilibrium photoexcitation processes or H_2 formation on grain surfaces may be occurring in the disk. If the H_2 lines are not in LTE, the fluorescent line ratios may be modified, possibly producing anomalous R_V values.

We calculate the total dust-to-gas ratio along the line of sight using our best-fit $A_V(H_2)$ and $N(H_2)$ values from this work and the H I column densities from McJunkin et al. (2014). Using $N_{H,tot} = N(HI) + 2N(H_2)$, we find $A_V(H_2)/N_{H,tot}$ ratios ranging from 0.5 to 25 times the canonical ISM value of $A_V/N_H = 5.3 \times 10^{-22}$ mag cm $^{-2}$ per H atom (Bohlin et al. 1978; Savage & Mathis 1979). A moderate amount of turbulence ($10^{-3} < \alpha_t < 10^{-2}$) could explain the larger dust-to-gas ratios. The turbulence could provide significant radial drift velocities to enrich the inner disk in dust, as well as provide a means to replenish the population of small grains through collisions (Birnstiel et al. 2012).

7. CONCLUSIONS

We find the best-fit UV extinction curve toward 16 protostars with circumstellar disks, correcting for molecular self-absorption in the disk, using a new H_2 fluorescence technique. Some targets are not well fit by a typical interstellar extinction curve, suggesting the occurrence of grain processing in the circumstellar environment or non-thermal H_2 level populations. H_2 column densities and temperatures are measured for these disks, and are generally consistent with previous H_2 line studies. We calculate $A_V(H_2)$ values higher than previous work based on H I column densities (McJunkin et al. 2014), and find little agreement with A_V values derived from optical and infrared measurements, which are themselves fairly disparate from each other. The methods likely probe different paths through the circumstellar material. Our fits generally do not find $R_V = 3.1$, meaning that comparisons with

the literature values that assume $R_V = 3.1$ may not be valid. We perform a second fit setting $R_V = 3.1$ and find A_V values that are more consistent for some targets and more inconsistent for others. This work is exploratory in developing a new technique, and part of that exploration is trying to figure out the limitations. One limitation is that our new technique likely needs A_V or R_V calculated independently to constrain the other because A_V and R_V are so highly degenerate. In future work, we hope to improve on the limitations of this new method and make it more robust.

APPENDIX ASSUMPTIONS IN $\text{Ly}\alpha$ RECONSTRUCTION

The reconstructed $\text{Ly}\alpha$ profiles used in this work to excite the H_2 molecules include certain assumptions. The fluorescing H_2 is assumed to be isothermal, which we also assume in this work and which is supported by recent modeling work from Ádámkovics et al. (2016), who find that including $\text{Ly}\alpha$ irradiation onto the disk atmosphere produces a region of hot (1500–2500 K) molecular gas that is hot enough to thermally excite the H_2 to vibrational levels capable of being pumped by $\text{Ly}\alpha$ photons. The H_2 gas that is absorbing and emitting in each progression is assumed to be well mixed, co-spatial, and at rest with respect to the star. The co-spatial assumption is necessary due to the fact that there is not a good prediction for the H_2 distribution in the disk. We use this assumption in our model as well to simplify the geometric dependence in the radiative transfer. H_2 gas located in the disk will have velocities that are not completely at rest with respect to the star due to thermal and turbulent broadening, as well as possible line-of-sight velocities if the gas is located in a disk wind. However, due to the observed, broad wings of the $\text{Ly}\alpha$ profile in most of the targets, even if the H_2 molecules have fairly large velocities with respect to the star (e.g., $\sim 20 \text{ km s}^{-1}$ in a disk wind; see Pontoppidan et al. 2011), this will not largely affect the reconstructed $\text{Ly}\alpha$ profiles for many of the stars because the profiles are essentially flat at these velocity scales.

Schindhelm et al. (2012b) do not account for the filling fraction (η) in their models, essentially assuming $\eta = 1$. This implies that the H_2 completely surrounds the star, which is unlikely. Herczeg et al. (2004) find $\eta = 0.25$ for TW Hya, while Wood et al. (2002) find $\eta > 2$ for Mira B, which possibly indicates the preferential scattering of $\text{Ly}\alpha$ photons out of, or H_2 photons into, our line of sight. Better treatment of this filling fraction is needed in future reconstructions of $\text{Ly}\alpha$ profiles. It is also assumed that H I is the only source of opacity between the stellar $\text{Ly}\alpha$ profile and the H_2 . H I is the most prevalent gas species between the star and the H_2 , producing a deep, broad absorption line. Other absorptions against the $\text{Ly}\alpha$ profile before reaching the H_2 would not be resolved by the rough resolution provided by the data points of the 12 progressions; and, as discussed in Section 5.1, the dust in this region is also negligible.

It is also assumed that the amount of H_2 that the $\text{Ly}\alpha$ travels into is the amount of H_2 that we observe. This is a necessary assumption because interstellar H I absorbs most of the stellar $\text{Ly}\alpha$ profile, so that we can only estimate the amount of $\text{Ly}\alpha$ radiation by measuring the H_2 fluorescence that it pumps. We underestimate the amount of H_2 in this assumption because the pumped H_2 fluoresces isotropically and may be emitted away from us, while some fluorescence lines also cannot escape as easily if not moving perpendicular to the disk. Lastly, it is

assumed that the entire $\text{Ly}\alpha$ profile reaches the H_2 in the disk equally. However, $\text{Ly}\alpha$ near the line center will be absorbed and scattered around by the nearby H I, such that it has a difficult time escaping, unlike $\text{Ly}\alpha$ away from the line center, which escapes easily. This will change the column density measured for each progression based on the location of the absorbing transition in the $\text{Ly}\alpha$ profile. This can be alleviated in future improvements to the fluorescence model where each progression is allowed to have a different column density and temperature.

REFERENCES

- Abgrall, H., Roueff, E., Launay, F., Roncin, J. Y., & Subtil, J. L. 1993a, *A&AS*, **101**, 273
- Abgrall, H., Roueff, E., Launay, F., Roncin, J. Y., & Subtil, J. L. 1993b, *A&AS*, **101**, 323
- Ádámkovics, M., Najita, J. R., & Glassgold, A. E. 2016, *ApJ*, **817**, 82
- Aikawa, Y., & Herbst, E. 1999, *A&A*, **351**, 233
- Alencar, S. H. P., Teixeira, P. S., Guimarães, M. M., et al. 2010, *A&A*, **519**, A88
- Allen, T. S., Prchlik, J. J., Megeath, S. T., et al. 2014, *ApJ*, **786**, 113
- Ardila, D. R., Basri, G., Walter, F. M., Valenti, J. A., & Johns-Krull, C. M. 2002, *ApJ*, **566**, 1100
- Argiroffi, C., Maggio, A., Montmerle, T., et al. 2012, *ApJ*, **752**, 100
- Bethell, T., & Bergin, E. 2009, *Sci*, **326**, 1675
- Birnstiel, T., Klahr, H., & Ercolano, B. 2012, *A&A*, **539**, A148
- Bohlin, R. C., Savage, B. D., & Drake, J. F. 1978, *ApJ*, **224**, 132
- Bruderer, S. 2013, *A&A*, **559**, A46
- Calvet, N., Muzerolle, J., Briceño, C., et al. 2004, *AJ*, **128**, 1294
- Cardelli, J. A., Clayton, G. C., & Mathis, J. S. 1989, *ApJ*, **345**, 245
- Cody, A. M., Tayar, J., Hillenbrand, L. A., Matthews, J. M., & Kallinger, T. 2013, *AJ*, **145**, 79
- Danforth, C. W., Keeney, B. A., Stocke, J. T., Shull, J. M., & Yao, Y. 2010, *ApJ*, **720**, 976
- Draine, B. T. 2003, *ARA&A*, **41**, 241
- Fitzpatrick, E. L. 1999, *PASP*, **111**, 63
- Fitzpatrick, E. L., & Massa, D. 2005, *AJ*, **130**, 1127
- Fitzpatrick, E. L., & Massa, D. 2007, *ApJ*, **663**, 320
- Fogel, J. K. J., Bethell, T. J., Bergin, E. A., Calvet, N., & Semenov, D. 2011, *ApJ*, **726**, 29
- France, K., Burgh, E. B., Herczeg, G. J., et al. 2012a, *ApJ*, **744**, 22
- France, K., Schindhelm, E., Bergin, E. A., Roueff, E., & Abgrall, H. 2014, *ApJ*, **784**, 127
- France, K., Schindhelm, E., Herczeg, G. J., et al. 2012b, *ApJ*, **756**, 171
- Furlan, E., Luhman, K. L., Espaillat, C., et al. 2011, *ApJS*, **195**, 3
- Güdel, M., Briggs, K. R., Arzner, K., et al. 2007, *A&A*, **468**, 353
- Gullbring, E., Hartmann, L., Briceno, C., & Calvet, N. 1998, *ApJ*, **492**, 323
- Hartigan, P., Edwards, S., & Ghandour, L. 1995, *ApJ*, **452**, 736
- Herbst, W., Herbst, D. K., Grossman, E. J., & Weinstein, D. 1994, *AJ*, **108**, 1906
- Herczeg, G. J., & Hillenbrand, L. A. 2014, *ApJ*, **786**, 97
- Herczeg, G. J., Linsky, J. L., Walter, F. M., Gahm, G. F., & Johns-Krull, C. M. 2006, *ApJS*, **165**, 256
- Herczeg, G. J., Walter, F. M., Linsky, J. L., et al. 2005, *AJ*, **129**, 2777
- Herczeg, G. J., Wood, B. E., Linsky, J. L., Valenti, J. A., & Johns-Krull, C. M. 2004, *ApJ*, **607**, 369
- Herzberg, G. 1950, *Molecular Spectra and Molecular Structure*, Vol. 1: Spectra of Diatomic Molecules (New York: Van Nostrand Reinhold)
- Hoadley, K., France, K., Alexander, R. D., McJunkin, M., & Schneider, P. C. 2015, *ApJ*, **812**, 41
- Jonkheid, B., Faas, F. G. A., van Zadelhoff, G.-J., & van Dishoeck, E. F. 2004, *A&A*, **428**, 511
- Lawson, W. A., Lyo, A.-R., & Muzerolle, J. 2004, *MNRAS*, **351**, L39
- Liu, W., & Dalgarno, A. 1996, *ApJ*, **467**, 446
- López-Santiago, J., Albacete Colombo, J. F., & López-García, M. A. 2010, *A&A*, **524**, A97
- Luhman, K. L., & Steeghs, D. 2004, *ApJ*, **609**, 917
- McJunkin, M., France, K., Schneider, P. C., et al. 2014, *ApJ*, **780**, 150
- Nomura, H., Aikawa, Y., Tsujimoto, M., Nakagawa, Y., & Millar, T. J. 2007, *ApJ*, **661**, 334
- Pontoppidan, K. M., Blake, G. A., & Smette, A. 2011, *ApJ*, **733**, 84
- Rieke, G. H., & Lebofsky, M. J. 1985, *ApJ*, **288**, 618

- Robrade, J., & Schmitt, J. H. M. M. 2007, [A&A](#), **473**, 229
- Rudnick, J. 1936, [ApJ](#), **83**, 394
- Savage, B. D., & Mathis, J. S. 1979, [ARA&A](#), **17**, 73
- Schindhelm, E., France, K., Burgh, E. B., et al. 2012a, [ApJ](#), **746**, 97
- Schindhelm, E., France, K., Herczeg, G. J., et al. 2012b, [ApJL](#), **756**, L23
- Schneider, P. C., Eisloffel, J., Güdel, M., et al. 2013, [A&A](#), **557**, A110
- Skinner, S. L., & Güdel, M. 2013, [ApJ](#), **765**, 3
- Stelzer, B., & Schmitt, J. H. M. M. 2004, [A&A](#), **418**, 687
- Testa, P., Huenemoerder, D. P., Schulz, N. S., & Ishibashi, K. 2008, [ApJ](#), **687**, 579
- Torres, C. A. O., Quast, G. R., Melo, C. H. F., & Sterzik, M. F. 2008, in Young Nearby Loose Associations, ed. B. Reipurth (San Francisco, CA: ASP), 757
- van Leeuwen, F. 2007, [A&A](#), **474**, 653
- Vasyunin, A. I., Wiebe, D. S., Birnstiel, T., et al. 2011, [ApJ](#), **727**, 76
- Welty, D. E., & Fowler, J. R. 1992, [ApJ](#), **393**, 193
- Woitke, P., Kamp, I., & Thi, W.-F. 2009, [A&A](#), **501**, 383
- Wolven, B. C., Feldman, P. D., Strobel, D. F., & McGrath, M. A. 1997, [ApJ](#), **475**, 835
- Wood, B. E., Karovska, M., & Raymond, J. C. 2002, [ApJ](#), **575**, 1057
- Yang, H., Linsky, J. L., & France, K. 2011, [ApJL](#), **730**, L10